Challenges in multiphysics modeling of dual-band HgCdTe infrared detectors

Challenges in multiphysics modeling of dual-band HgCdTe infrared detectors

MARCO VALLONE[1], MICHELE GOANO[1,2,*], ALBERTO TIBALDI[1,2], STEFAN HANNA[3], DETLEF EICH[3], ALEXANDER SIECK[3], HEINRICH FIGGEMEIER[3], GIOVANNI GHIONE[1], AND FRANCESCO BERTAZZI[1,2]

[1] *Politecnico di Torino, Dipartimento di Elettronica e Telecomunicazioni, Corso Duca degli Abruzzi 24, 10129 Torino, Italy*
[2] *IEIIT-CNR, corso Duca degli Abruzzi 24, 10129 Torino, Italy*
[3] *AIM Infrarot-Module GmbH, Theresienstraße 2, D-74072 Heilbronn, Germany*
[*] *Corresponding author: michele.goano@polito.it*

Compiled May 12, 2020

We present three-dimensional simulations of HgCdTe-based focal plane arrays (FPAs) with two-color and dual-band sequential infrared pixels having realistic truncated-pyramid shape, taking into account also the presence of compositionally-graded transition layers. After a validation against the spectral responsivity of two-color, mid-wavelength infrared detectors from the literature, the method has been employed for a simulation campaign on dual-band, mid- and long-wavelength infrared FPAs illuminated by a Gaussian beam. Simulation results underscore the importance of a full-wave approach to the electromagnetic problem, since multiple internal reflections due to metallizations and slanted sidewalls produce non-negligible features in the quantum efficiency spectra, especially in the long-wavelength band. Evaluations of the optical and diffusive contribution to inter-pixel crosstalk indicate the effectiveness of deep trenches to prevent diffusive crosstalk in both wavebands. In its present form, the detector seems to be subject to significant optical crosstalk in the long wavelength infrared band, which could be addressed through pixel shape optimization.

http://dx.doi.org/10.1364/ao.XX.XXXXXX

1. INTRODUCTION

Multispectral capability across infrared (IR) bands is a central requirement for third generation IR photodetectors [1–4]. Short, mid, long, and very long wavelength IR bands are conventionally defined respectively as: SWIR, $\lambda \in [1,3]\,\mu$m; MWIR, $\lambda \in [3,5]\,\mu$m; LWIR, $\lambda \in [8,14]\,\mu$m; VLWIR, $\lambda > 14\,\mu$m. The possibility to image a scene in two different IR bands [5], e.g. SWIR-MWIR or MWIR-LWIR (dual-band), or also in two subbands belonging to the same IR band (e.g. two-color MWIR-MWIR), offers the opportunity to determine the imaged object temperature, or to increase its contrast against the background, especially in presence of fog, haze, dust, and atmospheric turbulence. Outstanding properties of $Hg_{1-x}Cd_xTe$ (or MCT) [6–8] allow to fabricate large format dual-band or two-color focal plane arrays (FPAs) IR detectors, exploiting the degree of freedom offered by the largely x-tailorable MCT bandgap, gradually increasing from a negative value for HgTe to a positive value for CdTe, with an extremely small change of lattice constant.

In one of the simplest schemes, each pixel includes two stacked *p-n* absorbers, i.e., two back-to-back *p-n* photodiodes with different cut-off wavelength, separated by a thin, wide bandgap layer acting as barrier, and a single bias contact. This scheme is also known as *n-p-P-p-n* triple layer heterostructure, where the capital letter refers to the barrier, a thin layer with a bandgap wider than the absorbers. The shorter wavelength absorber is located closer to the illuminated detector face, and higher energy photons interact with it, leaving instead the lower energy photons to reach the longer wavelength section, located above and connected to the bias contact [1, 9–13]. In this class of detectors, known as sequential detectors, either of the *p-n* junction can be reverse biased by changing the polarity of the bias voltage, switching the spectral response between the two wavebands.

The development of multispectral IR-FPAs requires considerable design and technology effort in order to optimize quantum efficiency (QE), spatial and spectral crosstalk, high-temperature operability, spatial resolution, etc. Recent works [14–16] develop and employ multiphysics approach to reproduce single-color, compositionally graded HgCdTe IR photodetector performance, by means of combined three-dimensional (3D) electromagnetic and electrical simulations. In addition, simulations of 3D realistic pixel shapes require large numerical resources and careful choice of computational grid [17–23].

The application of the same procedure to two-color and dual-band FPAs is not straighforward, especially because of several numerical and implementation issues which arise when realistic pixel shapes are concerned: achieving fast and stable numerical 3D simulations is often non trivial, especially when heterostructures are concerned, in which carrier density drops to very small values due to reverse bias of semiconductor junctions. Hence, our first task has been the development and validation of the method against experimental results concerning a two-color detector described in good detail in literature

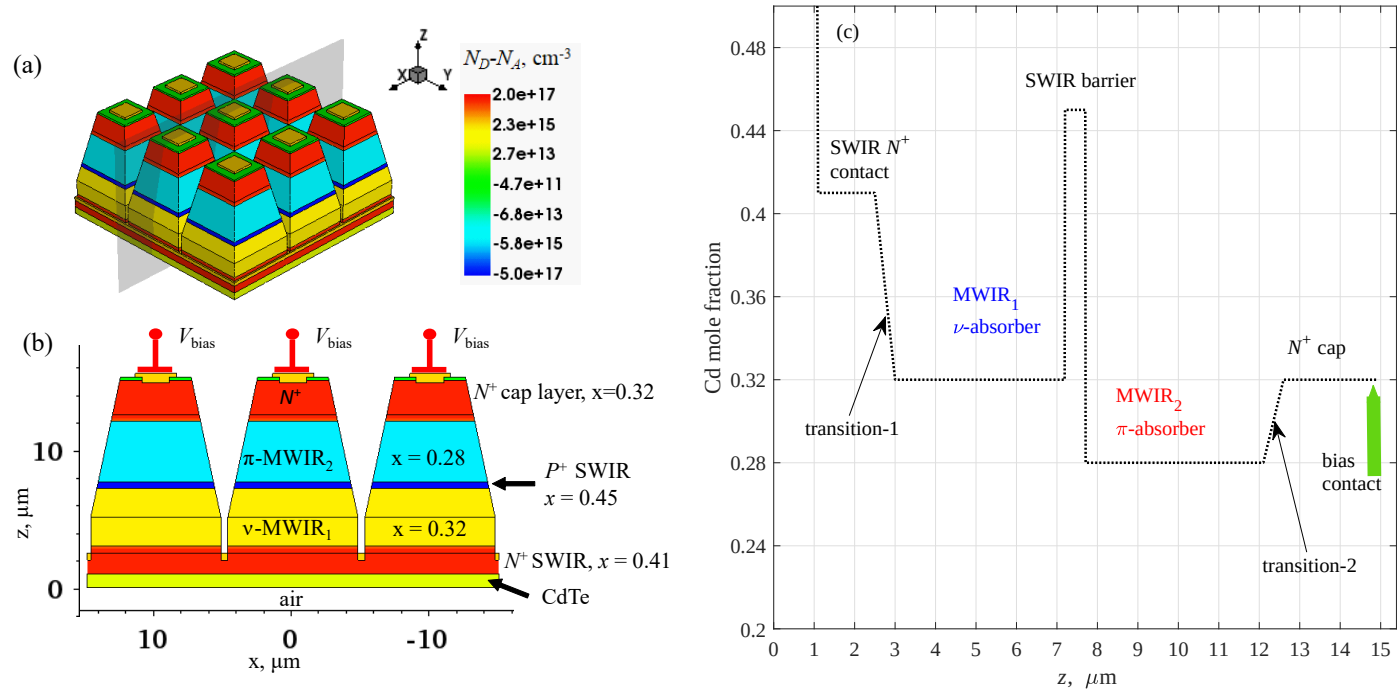

Fig. 1. (a) The 3D MWIR$_1$-MWIR$_2$ 3×3 miniarray, with a two dimensional (2D) cutplane (b) at center pixel showing the doping distribution $N_D - N_A$. (c) The composition profile along a one-dimensional (1D) cutline at center pixel.

[24, 25]. A description of the calculation method is given in Section 2, followed by its validation in Section 3.

After this preliminary step, we applied the same method to simulate a dual-band MWIR-LWIR detector operating at $T = 230$ K, and the obtained results and their discussion are presented in Section 4: for this value of temperature, a dark current below the "Rule 07" standard [26, 27] is predicted, even for the more challenging LWIR operation, without the necessity to consider too low and difficult to achieve doping levels. This is a lower bound that may represent an ideal target for high performance detectors. In fact, the present simulations do not include any effect of surface recombination, connections to the read-out circuit, noise, etc. Illuminating with a narrow Gaussian beam the central pixel (CP) of a 5×5 miniarray of pixels, we obtained useful indications about the optimal bias point for the selection of the MWIR and LWIR wavebands: the bias voltage should be large enough to provide low spectral crosstalk and high quantum efficiency [15, 16, 28–30], but not so large to trigger band-to-band tunneling.

2. METHOD OF CALCULATION

Electromagnetic (optical) and electric 3D simulations of HgCdTe-based IR-FPAs were performed considering $M \times M$ pixel miniarrays and employing a commercial numerical simulator by Synopsys [31], including an electromagnetic solver (EMW), and an electron transport solver (Sentaurus Device), here employed in the drift-diffusion approximation. The EMW section provides the solution of the electromagnetic problem for monochromatic illumination at wavelength λ according to the Finite Differences Time Domain (FDTD) method, after having discretized the miniarray into a 50 nm Yee grid [32, 33]. The FDTD method solves the Maxwell equations, and the electromagnetic solution is represented by the absorbed photon density A_{opt} (number of absorbed photons per unit volume and time), which is obtained as the divergence of the time-averaged Poynting vector $\langle \vec{S} \rangle$ [34–37]

$$A_{opt}(\lambda_n) = -\frac{\vec{\nabla} \cdot \langle \vec{S}(\lambda_n) \rangle}{hc/\lambda_n}. \quad (1)$$

Here h is the Planck constant, c is the light velocity in vacuum, and the material complex refractive index $n_r + i\kappa$ is included in $\vec{S}$ through Maxwell equations as shown e.g. in Refs. [29, 38], Eqs. (8-10). The optical generation rate distribution G_{opt} into the detector due to interband optical absorption is given by $G_{opt}(\lambda_n) = \eta A_{opt}(\lambda_n)$, where the quantum yield η, defined as the fraction of absorbed photons which are converted to photogenerated electron-hole pairs, was assumed to be unitary.

When a detector includes layers with compositional grading along the growth direction, a staircase discretization is required to overcome the limitations of the optical simulator [14], allowing to treat the complex refractive index as piecewise constant ([29], Table I). Only after this important step, the electromagnetic Yee's grid is built and the FDTD algorithm can provide the solution. Since a fine λ-sampling is important to describe and keep into account the rich resonance-like phenomenology around the cut-off-wavelength [14, 29], the wavelength interval should be sampled with fine enough resolution. Thus, a separate electromagnetic simulation followed by an electric simulation is required for each λ_n point, where G_{opt} enters as a source term in the electron and hole continuity equations, as described in detail e.g. in [38]. As a last remark, the staircase discretization should be fine enough to guarantee a small reflection coefficient between adjacent sublayers in the compositionally graded layers (see [14] for a discussion on this point).

3. VALIDATION ON MULTISPECTRAL DETECTORS

In order to validate the calculation method on multispectral detectors, we simulated the 3×3 MWIR$_1$-MWIR$_2$ miniarray shown in Fig. 1, where the compositional profile and the doping scheme along the growth direction z was kept as similar as possible to the structure from Ref. [25], one among the few literature contributions which report detailed experimental measurements and photodetector characteristics. The detector is a heterostructure with doping scheme $N^+ - \nu - P^+ - \pi - N^+$ (conventionally, lower case Greek letters re-

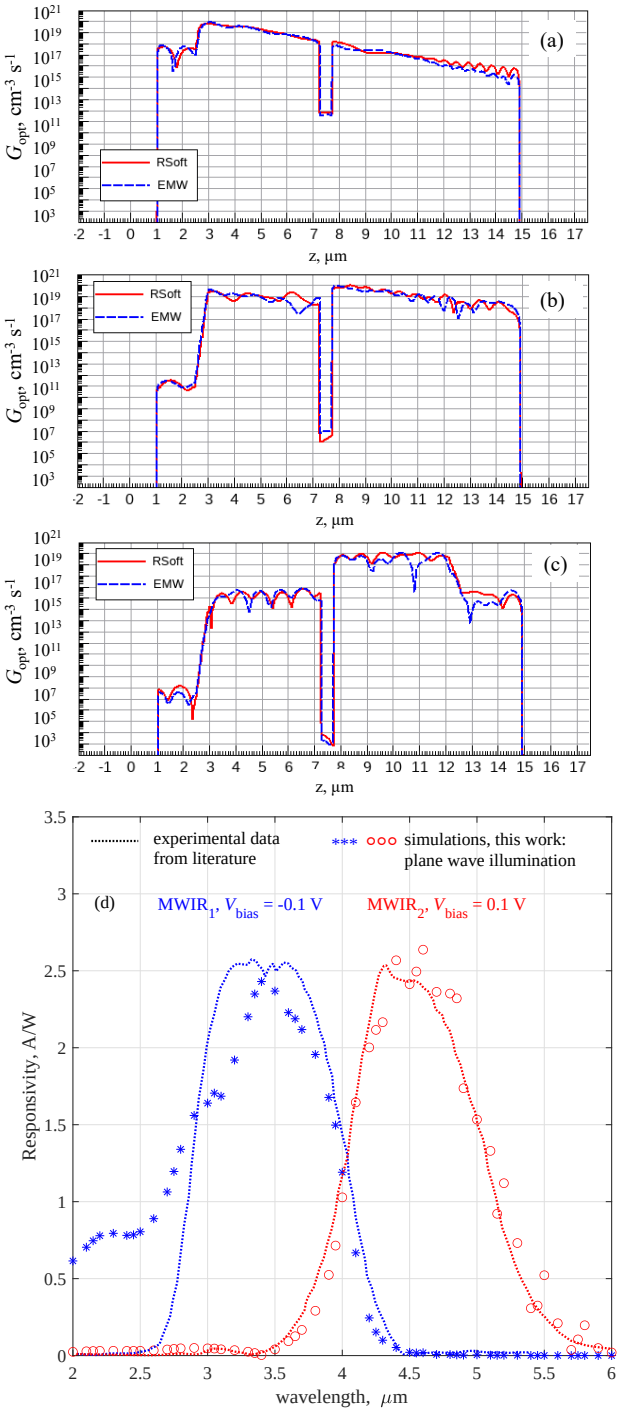

Fig. 2. The optical generation rates G_{opt}, evaluated with EMW and FullWAVE-RSoft simulators (1D cutlines at center miniarray, along the z-axis), for (a) $\lambda_n = 3\,\mu$m , (b) $\lambda_n = 4\,\mu$m, and (c) $\lambda_n = 5\,\mu$m. (d) Simulated spectral responsivity for plane wave illumination (symbols), with the experimental curves, obtained from [Fig. 2, 25], superimposed on the same figure (dotted lines).

fer to low-doped absorber regions, whereas upper case letters refer to layers with a bandgap wider than absorbers). It is composed by a 1.5 μm-thick $Hg_{0.59}Cd_{0.41}Te$ N^+-SWIR donor doped ($N_D = 2\times10^{17}$ cm^{-3}) contact layer grown on a CdTe substrate, followed by two ν- and π-absorbers with different bandgap and doping, separated by a P^+-SWIR barrier, and by a 2.5 μm-thick $Hg_{0.68}Cd_{0.32}Te$ donor-doped ($N_D = 2\times10^{17}$ cm^{-3}) cap layer. In the present work, the ν- and π-absorbers are respectively a 4.2 μm-thick low donor-doped ($N_D = 10^{15}$ cm^{-3}) $Hg_{0.68}Cd_{0.32}Te$ (MWIR$_1$) and a 4.4 μm-thick low acceptor-doped ($N_A = 5\times10^{15}$ cm^{-3}) $Hg_{0.72}Cd_{0.28}Te$ (MWIR$_2$) layer, and they are separated by a 0.5 μm-thick acceptor-doped ($N_A = 5\times10^{17}$ cm^{-3}) $Hg_{0.55}Cd_{0.45}Te$ P^+-SWIR barrier. To provide a realistic description of the geometry, a 0.5 μm-thick transition layer with linear composition profile is inserted to connect the SWIR contact layer to the MWIR$_1$ absorber, and another similar one connects the MWIR$_2$ absorber to the cap layer, as shown in Fig. 1(c).

The pixels are defined by triangular trenches, and their shape is a truncated pyramid with 10 μm wide square base. The angle of the mesa sidewalls is set to 78° respect to the plane $Z = 0$, a value that should assure total reflection at the sidewalls in a large interval of incident radiation wavevector directions [28]. A metal ring surrounds the perimeter of pixels, it is connected to the contact layers, providing a common ground for all them. The cap layer of each pixel is connected to a square metallic layer (the bias contact), partly extending over a 0.3 μm thick CdTe passivation layer that covers the pixel upper face.

The dependence of HgCdTe properties on composition, doping and temperature was taken into account according to the models reported in Ref. [29], without including possible doping-induced plasma effects in the complex refractive index, e.g., Burstein-Moss effect and free carrier absorption, [39, 40]. The Shockley-Read-Hall (SRH) recombination processes were modeled as in Ref. [41] considering a lifetime around 100 μs, neglecting for simplicity trap-assisted tunneling [42–44], but keeping into account possible contributions to generation-recombination rate coming from band-to-band tunneling (BTBT), described according to the classical expression by Kane [45]

$$R_{\mathrm{BTBT,\,Kane}} = \frac{np - n_i^2}{(n+n_i)\,(p+n_i)} A\mathscr{E}^2 \exp\left(\frac{B}{\mathscr{E}}\right) \qquad \textbf{(2)}$$

where, for parabolic barriers, the A and B coefficients are [46, 47]

$$A = -\frac{q\sqrt{2m_e}}{4\pi^3\hbar^2\sqrt{E_g}}, \quad B = \frac{\pi\sqrt{m_e E_g^3}}{2\sqrt{2}\,q\hbar} \qquad \textbf{(3)}$$

$\mathscr{E}$, E_g, m_e, q and $\hbar$ being respectively the local electric field, energy gap, electron effective mass, electron charge and reduced Planck's constant, n_i, n, and p respectively the intrinsic, electron and hole densities. Alternative expressions, that treat less idealized cases, accounting e.g. for the Fermi levels position in the neutral regions [48] or considering 2D and 3D realistic junction profiles [41, 46, 47] may be also employed. However, since all these models make use of fitting parameters, in absence of any experimental data we preferred to apply the classical Kane's expression in Eq. (2). Fermi-Dirac statistics and incomplete dopant ionization were taken into account, with activation energies for HgCdTe alloys estimated according to [49, 50]. The computational box included air layers located above and below the miniarray (instead of other filling material, for simplicity), and the optical boundary conditions have been set as absorbing along z (this is obtained with convolutional perfectly matching layers [51]), and periodic along x and y, in order to mimic an infinitely extended pixel array.

The detector was simulated in dark and under monochromatic plane wave illumination, considering a propagation vector orthogonal to the detector horizontal plane $z = 0$. The power flux was set to 1 mW cm^{-2}, and the wavelength was varied in the interval $\lambda \in [2, 6]\,\mu$m, with a sampling step of 0.1 μm. Temperature has been set to $T = 230$ K.

In Fig. 2(a-c) we compare the electromagnetic solution obtained with EMW and with an independent electromagnetic solver, the RSoft FullWAVE [52], for three representative wavelengths, one chosen in the MWIR$_1$ band ($\lambda = 3\,\mu$m), one in the MWIR$_2$ band ($\lambda = 5\,\mu$m), and

one in between, where the spectral crosstalk in maximum ($\lambda = 4\,\mu$m). The agreement is satisfactory, therefore we employed EMW for all the rest of the campaign.

In Fig. 2(d) we show the simulated spectral responsivity, obtained as described in this Section and defined as $I_{ph,\mathrm{CP}}/P$, where $I_{ph,\mathrm{CP}}$ and P are, respectively, the photocurrent collected by the CP contact and the optical power impinging on the CP. The experimental curves obtained from [Fig. 2, 25] have been plotted on the same figure for comparison (no parameters or normalization constants have been employed to fit simulations and experimental data). Although we ignore the true pixel shape of the experimental realization in Ref. [25], we can notice the general similarity between experimental and simulated curves: they share some interesting small detail, like the maximum obtained responsivity in both bands, the very small bump at $\lambda \approx 3\,\mu$m in the MWIR_2 spectrum, and the same wavelength $\lambda \approx 4\,\mu$m at which the MWIR_1 and MWIR_2 spectra cross each other. However, it is remarkable the bump for $\lambda \approx 2.25\,\mu$m visible only in the present simulation, probably due to different ground contact position and extension, different pixel shape, trench depth, etc.

4. DUAL-BAND MWIR-LWIR DETECTOR WITH GAUSSIAN BEAM ILLUMINATION

The main purpose of the present work is to employ the described multiphysics simulation scheme to design a dual-band detector, obtained as a variant of the detector considered so far. In this case and differently from what described in Section 3, we considered a 5×5 MWIR-LWIR miniarray illuminated from below by a narrow Gaussian beam, with the beam axis orthogonal to the detector horizontal plane xy, centered on the miniarray CP and focused on the illuminated face. The beam power flux profile is $\Phi(r) = \Phi_0 \exp\left(-2r^2/w_0^2\right)$, where Φ_0 is the optical power flux along the beam axis, r is the radial distance from the beam axis and $w_0 = 2.5\,\mu$m is the beam waist radius. It must be noticed that $\Phi(r)$ never goes to zero, hence the beam tail partially illuminates also the CP neighboring pixels. The need for a 5×5 miniarray, instead of a simpler 3×3, is due to an increase of calculation accuracy required to describe the inter-pixel crosstalk [28, 30] and the complex interference effects due to internal reflections, more prominent in LWIR detectors, for which the wavelength is in the order of the pixel pitch [29, 35]. The simulated 5×5 MWIR-LWIR miniarray is shown in Fig. 3(a). The layers thickness is the same adopted for the MWIR_1-MWIR_2, except for the cap layer, that is considerably thinner (its thickness is $0.5\,\mu$m, instead of $2.5\,\mu$m). The dopant concentrations in all the layers are the same as for the MWIR_1-MWIR_2 detector, as well as the pixel pitch and sidewalls angle.

The Cd mole fraction in the absorbers was set to $x = 0.295$ (MWIR) and $x = 0.19$ (LWIR), whereas its optimal value x_{barr} in the P^+-SWIR barrier was determined by a set of simulations. The primary task of the barrier is to prevent effectively most of carrier flow between the two sections, so that an optimal choice of its bandgap is of crucial importance. To this end, we simulated the MWIR-LWIR detector in dark, considering five values of x_{barr} in the interval $[0.3, 0.5]$ (the bandgap increases roughly linearly with x_{barr}). In the electron and hole continuity equations we included, as generation-recombination terms, the Auger, SRH and BTBT as in Section 3, and in all the simulations the temperature was set to $T = 230$ K.

The simulated dark currents obtained with the considered values of x_{barr} are shown in Fig. 3(b). First we observe that the dark current is strongly affected by the barrier height, which decreases by two orders of magnitude when x_{barr} increases in the considered interval. However, we can notice that for $x_{\mathrm{barr}} > 0.40$ the dark current does not decrease further, therefore we set out to adopt, for all the simulations that follow, $x_{\mathrm{barr}} = 0.45$ as a conservative value, as done for the MWIR_1-MWIR_2 detector.

An interesting feature is the dark current peak for $V_{\mathrm{bias}} \approx 0.15$ V, followed by a decrease to a flat minimum in $0.25\,V < V_{\mathrm{bias}} < 0.6$ V. The current reduction for increasing reverse bias is due to the progressive extension of a carrier depleted region around the LWIR junction: absorber depletion of carriers in double-layer planar heterostructures is a mechanism that has been indicated as a method to suppress Auger generation, and it has been widely studied by several groups [53–56]. An extensive discussion about this important point, and especially about its implication in the reduction of inter-pixel crosstalk under illumination has been provided in recent works for single-band detectors [15, 16]. An extension of this concept to dual-band detectors is an important point, and it is worth of a separate investigation, now undergoing.

Although for positive bias the dark current is more than three orders of magnitude higher than for negative bias, if $V_{\mathrm{bias}} < 0.6$ V its value never exceeds the reference value given by the "Rule07" [26, 27], reported in the inset of Fig. 3(b) for the LWIR absorber material (the symbol refers to $T = 230$ K).

A further important point is that, for $V_{\mathrm{bias}} > 0.6$ V, a non-negligible BTBT contribution is clearly present, in contrast to what happens for the MWIR section. Thus, with regard to simulations with illumination, when considering positive bias in order to select the LWIR band, it is highly advisable to choose a voltage below this value, also avoiding the interval $0.1 \lessapprox V_{\mathrm{bias}} \lessapprox 0.25$ V around the dark current peak. Hence, good choices are in the interval $V_{\mathrm{bias}} \in [0.25, 0.6]$ V.

For negative applied voltage, there is no sign of BTBT contributions, but since the dark current is already in saturation for $V_{\mathrm{bias}} \approx -0.1$ V, this bias value should be a good choice for MWIR operation.

In order to check the correct polarization with the selected values for V_{bias}, in Fig. 4 we show the band diagrams in dark. When the applied bias voltage is $V_{\mathrm{bias}} = -0.1$ V, the two absorber sections are respectively in reverse polarization (MWIR) and in quasi-equilibrium (LWIR, see the quasi-superimposed electron and hole Fermi levels). Conversely, for $V_{\mathrm{bias}} = 0.3$ V (a value in the recommended interval for LWIR operation, as discussed above), the MWIR section is in forward bias (but the barrier prevents electrons leakage towards the LWIR section), whereas the LWIR section is reverse biased, as apparent from Fermi levels position. Hence, the detector, when illuminated, is expected to work correctly in sequential mode with the indicated values of $V_{\mathrm{bias}} = -0.1$ V and 0.3 V.

Following the same simulation scheme outlined in Section 2 and validated in Section 3, we simulated the MWIR-LWIR detector illuminated by a Gaussian beam on the miniarray CP as described above, for $V_{\mathrm{bias}} = -0.1$, 0.3, 0.5 V, and in Fig. 5 the obtained spectral QE is shown ($\mathrm{QE} = hc/(q\lambda) I_{ph,\mathrm{CP}}/P$). For $V_{\mathrm{bias}} = -0.1$ V the spectral response is, as expected, in the MWIR band, with maximum QE above 0.8, and MWIR cut-off at $\lambda_{\mathrm{c,\,MW}} \approx 4.5\,\mu$m. A positive voltage $V_{\mathrm{bias}} = 0.3$ V provides a good spectral response in the LWIR band with a maximum QE around 0.75 and a LWIR cut-off at $\lambda_{\mathrm{c,\,LW}} \approx 9.7\,\mu$m. Moreover, considering positive bias, if V_{bias} is raised to 0.5 V, the BTBT generation should not be triggered yet, at least according to the present model (see Fig. 3(b)), nevertheless this does not provide significant increase of QE, and should be avoided.

In the LWIR waveband, it is also possible to observe a consistent spectral QE oscillation, not present in the MWIR band, due to the backreflections at the contact metallization and at the pyramidal pixel sidewalls, making interference effects a non-negligible characteristic. As pointed out in previous works [29, 38], the effects of multiple reflections and quasi-standing wave behavior are particularly important when the material tends to become semi-transparent and the wavelength is in the order of the pixel size.

Another important point is the inter-pixel crosstalk [28, 29]: very generally and with reference to Fig. 3(a), the inter-pixel crosstalk is

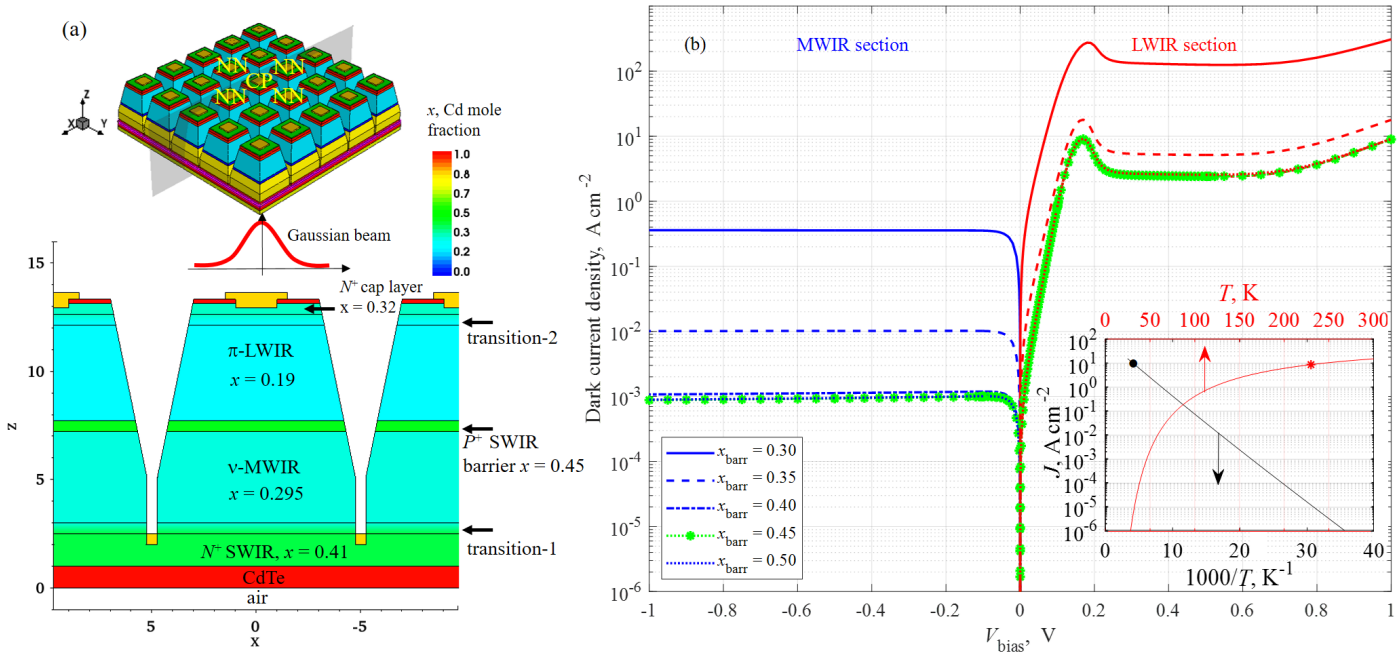

Fig. 3. (a) The simulated dual-band 5×5 MWIR-LWIR miniarray, with the central pixel (CP) and the nearest neighboring pixels (NNs). (b) The dark current density, simulated for five values of barrier composition x_{barr}. In the inset, the "Rule07" dark current density J vs. temperature is shown for the LWIR absorber material $Hg_{0.81}Cd_{0.19}Te$ (the symbols refer to $T = 230$ K).

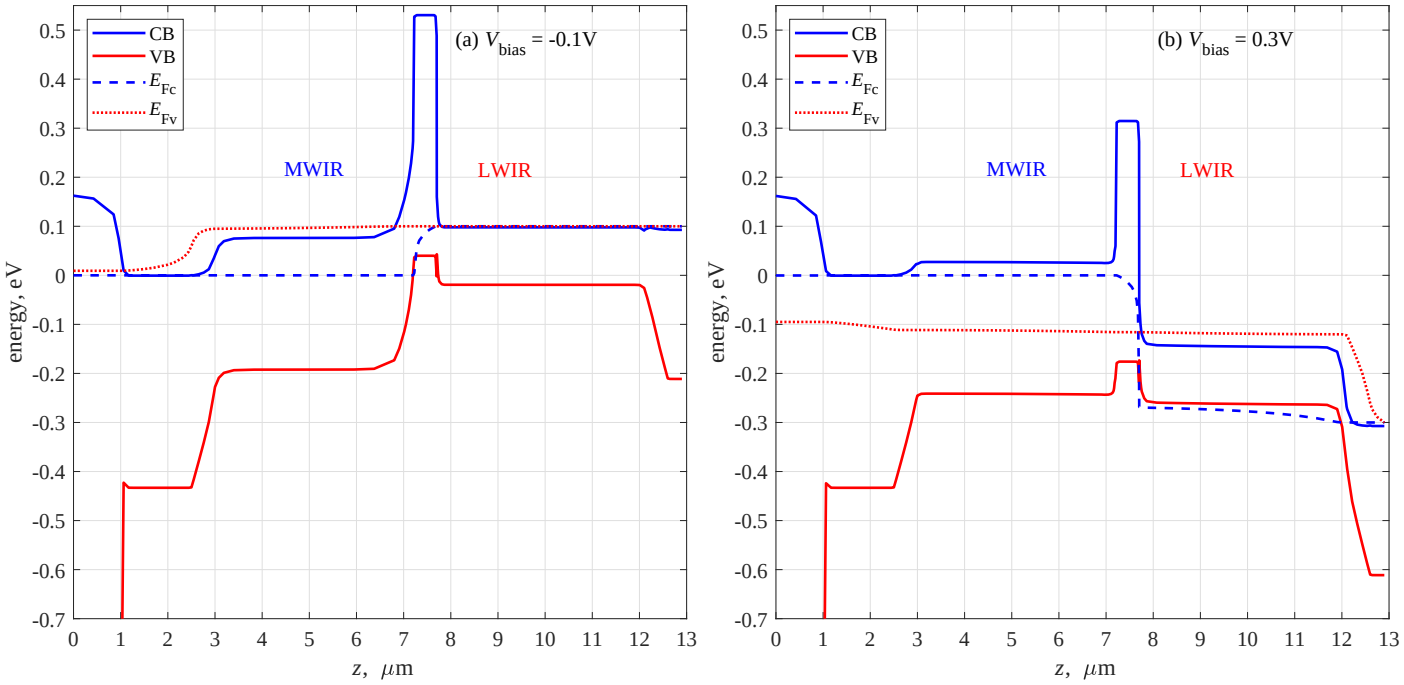

Fig. 4. The MWIR-LWIR detector band diagrams when the applied bias V_{bias} is -0.1 V (panel (a)) or 0.3 V (panel(b)), showing the conduction band (CB), the valence band (VB), the electron E_{Fc} and hole E_{Fv} Fermi levels.

the photoresponse of nearest neighboring pixels (NNs) to a beam illuminating the CP. In the present work, we adopted the definitions for the "total" $\mathscr{C}_{NNs}$, "optical" $\mathscr{O}_{NNs}$ and "diffusive" $\mathscr{D}_{NNs}$ contributions to the crosstalk

$$\mathscr{C}_{\mathrm{NNs}} = \frac{I_{ph,\mathrm{NNs}}}{I_{ph,\mathrm{CP}}}, \quad \mathscr{O}_{\mathrm{NNs}} = \frac{\int_{V_{\mathrm{NNs}}} G_{\mathrm{opt}}(x,y,z)\,dxdydz}{\int_{V_{\mathrm{CP}}} G_{\mathrm{opt}}(x,y,z)\,dxdydz},$$
$$\mathscr{D}_{\mathrm{NNs}} \approx \mathscr{C}_{\mathrm{NNs}} - \mathscr{O}_{\mathrm{NNs}}, \qquad (4)$$

introduced and extensively discussed in [30] ($I_{ph,\mathrm{NNs}}$ is the photocurrent collected by the NNs; V_{CP} and V_{NNs} are the CP and NNs pixel volumes). In short, the "optical" crosstalk $\mathscr{O}_{\mathrm{NNs}}$ is due to carriers photogenerated in the NNs by the Gaussian beam tails and by light possibly scattered from the CP to the NNs, and collected by their contacts. The "total" crosstalk $\mathscr{C}_{\mathrm{NNs}}$ includes contributions coming from $\mathscr{O}_{\mathrm{NNs}}$, but also from carriers photogenerated in the CP, diffused into the NNs,

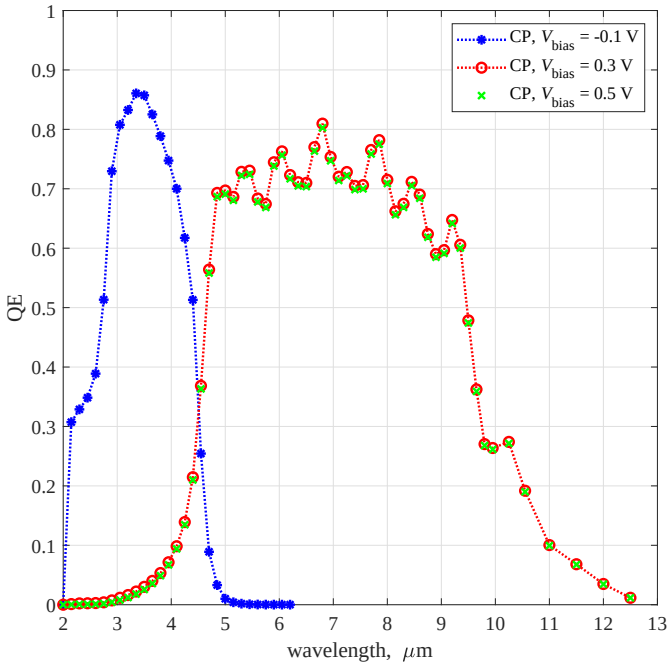

Fig. 5. Spectral QE (adimensional) of the dual-band MWIR-LWIR detector, for Gaussian beam illumination centered on the miniarray CP, for several values of the bias voltage. The optimal bias is -0.1 V for MWIR and 0.3 V for LWIR operation.

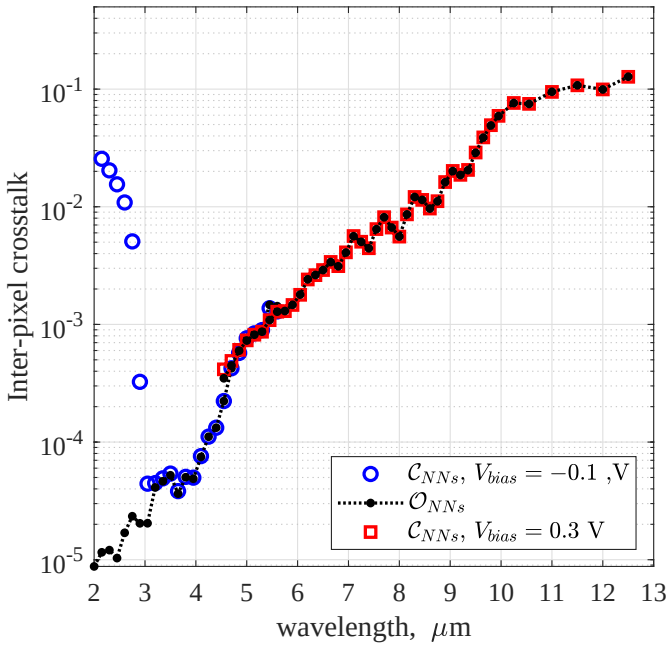

Fig. 6. The "total" $\mathscr{C}_{NNs}$ and "optical" $\mathscr{O}_{NNs}$ spectral inter-pixel crosstalk (adimensional) in the present MWIR-LWIR photodetector.

and collected by their contacts: this is the "diffusive" crosstalk $\mathscr{D}_{\mathrm{NNs}}$, approximatively given by the difference $\mathscr{C}_{\mathrm{NNs}} - \mathscr{O}_{\mathrm{NNs}}$ [30]. An important point is the beam evolution: far from its focal plane, the beam cone angle can be estimated with the paraxial approximation to be [57] $\vartheta \approx \lambda/(\pi n_r w_0)$. In absence of technological solutions limiting this occurrence, like e.g. metalenses [58], we may expect $\mathscr{O}_{\mathrm{NNs}}$ to increase linearly with λ. $\mathscr{O}_{\mathrm{NNs}}$ constitutes a non negligible contribution, to be calculated in conjunction with $\mathscr{C}_{\mathrm{NNs}}$ in order to evaluate correctly the contribution of diffusion to crosstalk, $\mathscr{D}_{\mathrm{NNs}}$.

In Fig. 6 we plot the spectral inter-pixel crosstalk $\mathscr{C}_{\mathrm{NNs}}$ and $\mathscr{O}_{\mathrm{NNs}}$ for MWIR and LWIR operation. Regarding the LWIR operation, the deep trenches do not allow carriers, photogenerated by LWIR photons in the upper part of the detector, to migrate into one of the NNs. Therefore, the LWIR band is expected to have negligible diffusive crosstalk, with $\mathscr{C}_{\mathrm{NNs}} \approx \mathscr{O}_{\mathrm{NNs}}$, as shown in Fig. 6 for the curves for $V_{\mathrm{bias}} = 0.3$ V (red squares and black points). However, it is evident that in this waveband the detector shows significant optical crosstalk, whose reduction possibly requires the optimization of the pixel shape, in order to avoid the fast rise of $\mathscr{O}_{\mathrm{NNs}}$ for increasing λ. Conversely, for the MWIR operation, minority carriers (holes) photogenerated into the MWIR section have, in principle, better chances to diffuse laterally. However, in order to migrate from the CP into one of the NNs, they should overcome the ≈ 200 meV barrier between the N^+-SWIR contact layer and the ν-MWIR absorber. Thanks to this barrier, also for $\lambda \in [3, 5]\,\mu$m the total crosstalk $\mathscr{C}_{NNs}$ is very close to $\mathscr{O}_{NNs}$ (Fig. 6, blue circles and black points), hence the diffusive crosstalk is very small.

A different situation takes place for $\lambda < 3\,\mu$m: most photons are absorbed by the N^+-SWIR contact layer before reaching the MWIR section, and it is more likely for them to diffuse towards NNs, since this layer is quasi-neutral. Actually, Fig. 6 shows that, when λ is progressively reduced below $3\,\mu$m, the total inter-pixel crosstalk $\mathscr{C}_{\mathrm{NNs}}$ increases considerably, as its optical contribution $\mathscr{O}_{\mathrm{NNs}}$ progressively decreases: for $\lambda \approx 2\,\mu$m, the crosstalk is almost diffusive. This fact can be an interesting input for a future investigation campaign, involving the effect of the depth of trenches that define the pixels: if trenches are more shallow and do not insulate all the MWIR section, differently from the present case, a substantial diffusive crosstalk could be expected also in the MWIR waveband.

5. CONCLUSIONS

We developed a simulation method suitable to investigate HgCdTe-based two-color and dual-band IR-FPAs with realistic 3D truncated-pyramidal pixel shape. The method is very general since, with an appropriate layer discretization, it solves the Maxwell equations under arbitrary illumination, also in presence of epitaxial layers with compositional grading, a non trivial issue for most commercial electromagnetic solvers. The subsequent solution of the electrical problem under illumination was treated in the drift-diffusion approximation, and it allowed to validate the method against literature data [25], reproducing experimental responsivity spectra of two-color MWIR-MWIR detectors.

The method has been employed for a preliminary study of dual-band FPA MWIR-LWIR detector illuminated by a Gaussian beam, characterizing its spectral quantum efficiency and identifying the different dominant sources of inter-pixel crosstalk in the different wavebands. The combined electromagnetic and electrical simulations indicate the importance to treat with a full-wave method the electromagnetic problem, since the effects of multiple internal reflections due to metallization and pyramidal pixel sidewalls produce important QE spectral features especially in the LWIR band.

This methodology paves the way towards the study of the effects of pixel pitch, trench depth, contact layer thickness, and angle of the pixel sidewalls, expected to affect both the spectral QE and the spatial inter-pixel crosstalk, which are going to be investigated in future works along with the effects of the absorber doping and its possible compositional grading, which has been shown to be important in single color detectors [16].

Simulations state a lower limit for the dark current in absence of

nonidealities (except for SRH), and indicate the key role of the deep trenches in preventing the diffusive crosstalk in both wavebands. Their effectiveness can be understood also considering the rapid increase of total crosstalk for $\lambda < 3\,\mu$m: in this case most photons are absorbed by the N^+-SWIR contact layer before reaching the MWIR section, and it is more likely for them to diffuse towards NNs, exactly because of the absence of trenches in this layer. Simulations also indicate that an optimization of the pixel shape is advisable, in order to avoid the fast rise of $\mathscr{O}_{\mathrm{NNs}}$ for increasing λ.

6. DISCLOSURES

Disclosures. The authors declare no conflicts of interest.

REFERENCES

1. A. Rogalski, "HgCdTe infrared detector material: history, status and outlook," Rep. Prog. Phys. **68**, 2265–2336 (2005).
2. P. Martyniuk, J. Antoszewski, M. Martyniuk, L. Faraone, and A. Rogalski, "New concepts in infrared photodetector designs," Appl. Phys. Rev. **1**, 041102 (2014).
3. O. Gravrand, J. Rothman, C. Cervera, N. Baier, C. Lobre, J. P. Zanatta, O. Boulade, V. Moreau, and B. Fieque, "HgCdTe detectors for space and science imaging: general issues and latest achievements," J. Electron. Mater. **45**, 4532–4541 (2016).
4. R. K. Bhan and V. Dhar, "Recent infrared detector technologies, applications, trends and development of HgCdTe based cooled infrared focal plane arrays and their characterization," Opto-Electron. Rev. **27**, 174–193 (2019).
5. D. Eich, C. Ames, R. Breiter, H. Figgemeier, S. Hanna, H. Lutz, K. Mahlein, T. Schallenberg, A. Sieck, and J. Wenish, "MCT-based high performance bispectral detectors by AIM," J. Electron. Mater. **48**, 6074–6083 (2019).
6. M. A. Kinch, "Fundamental physics of infrared detector materials," J. Electron. Mater. **29**, 809–817 (2000).
7. M. A. Kinch, "HgCdTe: Recent trends in the ultimate IR semiconductor," J. Electron. Mater. **39**, 1043–1052 (2010).
8. M. Reine, "Interview with Paul W. Kruse on the early history of HgCdTe, conducted on October 22, 1980," J. Electron. Mater. **44**, 2955–2968 (2015).
9. J. M. Arias, M. Zandian, G. M. Williams, E. R. Blazejewski, R. E. DeWames, and J. R. Pasko, "Hgcdte dual-band infrared photodiodes grown by molecular beam epitaxy," J. Appl. Phys. **70**, 4620–4622 (1991).
10. P. Ballet, F. No'el, F. Pottier, S. Plissard, J. P. Zanatta, J. Baylet, O. Gravrand, E. D. Borniol, S. Martin, P. Castelein, J. Chamonal, A. Million, and G. Destefanis, "Dual-band infrared detectors made on high-quality HgCdTe epilayers grown by molecular beam epitaxy on CdZnTe or CdTe/Ge substrates," J. Electron. Mater. **33**, 667–672 (2004).
11. R. A. Coussa, A. M. Gallagher, K. Kosai, L. T. Pham, G. K. Pierce, E. P. Smith, G. M. Venzor, T. J. D. Lyon, J. E. Jensen, B. Z. Nosho, J. A. Roth, and J. R. Waterman, "Spectral crosstalk by radiative recombination in sequential-mode, dual mid-wavelength infrared band HgCdTe detectors," J. Electron. Mater. **33**, 517–525 (2004).
12. J. Ziegler, D. Eich, M. Mahlein, T. Schallenberg, R. Scheibner, J. Wendler, J. Wenisch, R. Wollrab, V. Daumer, R. Rehm, F. Rutz, and M. Walther, "The development of 3rd gen IR detectors at AIM," in *Infrared Technology and Applications XXXVII,* vol. 8012, Proceedings of the SPIE B. F. Andresen, G. F. Fulop, and P. R. Norton, eds. (2011), p. 801237.
13. R. K. McEwen, L. Hipwood, S. Bains, D. Owton, and C. Maxey, "Dual waveband infrared detectors using MOVPE grown MCT," in *Detectors and Imaging Devices: Infrared, Focal Plane, Single Photon,* vol. 11002, Proceedings of the SPIE (2019), p. 1100218.
14. M. Vallone, M. Goano, F. Bertazzi, G. Ghione, S. Hanna, D. Eich, and H. Figgemeier, "FDTD simulation of compositionally graded HgCdTe photodetectors," Infrared Phys. Tech. **97**, 203–209 (2019).
15. M. Vallone, M. Goano, F. Bertazzi, G. Ghione, S. Hanna, D. Eich, and H. Figgemeier, "Reducing inter-pixel crosstalk in HgCdTe detectors," Opt. Quantum Electron. **52**, 25 (2020).
16. M. Vallone, M. Goano, F. Bertazzi, G. Ghione, S. Hanna, D. Eich, A. Sieck, and H. Figgemeier, "Constraints and performance tradeoffs in Auger-suppressed HgCdTe focal plane arrays," Appl. Opt. **59**, E1–E8 (2020).
17. D. D'Orsogna, S. P. Tobin, and E. Bellotti, "Numerical analysis of a very long-wavelength HgCdTe pixel array for infrared detection," J. Electron. Mater. **37**, 1349–1355 (2008).
18. J. Schuster and E. Bellotti, "Analysis of optical and electrical crosstalk in small pitch photon trapping HgCdTe pixel arrays," Appl. Phys. Lett. **101**, 261118 (2012).
19. E. Bellotti, J. Schuster, B. Pinkie, and F. Bertazzi, "Multi-scale modeling of photon detectors from the infrared to the ultraviolet," in *Infrared Sensors, Devices, and Applications III,* vol. 8868, Proceedings of the SPIE (2013), p. 88680R.
20. B. Pinkie and E. Bellotti, "Large-scale numerical simulation of reduced-pitch HgCdTe infrared detector arrays," in *Infrared Technology and Applications XXXIX,* vol. 8704, Proceedings of the SPIE (2013), p. 87042S.
21. J. Schuster, B. Pinkie, S. Tobin, C. Keasler, D. D'Orsogna, and E. Bellotti, "Numerical simulation of third-generation HgCdTe detector pixel arrays," IEEE J. Sel. Top. Quantum Electron. **19**, 800415 (2013).
22. M. Vallone, M. Goano, F. Bertazzi, G. Ghione, R. Wollrab, and J. Ziegler, "Modeling photocurrent spectra of single-color and dual-band HgCdTe photodetectors: Is 3D simulation unavoidable?" J. Electron. Mater. **43**, 3070–3076 (2014).
23. R. DeWames, R. Littleton, K. Witte, A. Wichman, E. Bellotti, and J. Pellegrino, "Electro-optical characteristics of P^+n <$In_{0.53}Ga_{0.47}As$ hetero-junction photodiodes in large format dense focal plane arrays," J. Electron. Mater. **44**, 2813–2822 (2015).
24. P. Martyniuk, P. Madejczyk, W. Gawron, and J. Rutkowski, "Demonstration of a dual-band mid-wavelength HgCdTe detector operating at room temperature," J. Electron. Mater. **47**, 5752–5758 (2018).
25. M. Kopytko, W. Gawron, A. Kębłowski, D. Stępieź, P. Martyniuk, and K. Jóźwikowski, "Numerical analysis of HgCdTe dual-band infrared detector," Opt. Quantum Electron. **51**, 62 (2019).
26. W. E. Tennant, D. Lee, M. Zandian, E. Piquette, and M. Carmody, "MBE HgCdTe technology: A very general solution to IR detection, described by "Rule 07", a very convenient heuristic," J. Electron. Mater. **37**, 1406–1410 (2008).
27. W. E. Tennant, ""Rule 07" revisited: still a good predictor of p/n HgCdTe photodiode performance?" J. Electron. Mater. **39**, 1030–1035 (2010).
28. B. Pinkie and E. Bellotti, "Numerical simulation of spatial and spectral crosstalk in two-color MWIR/LWIR HgCdTe infrared detector arrays," J. Electron. Mater. **42**, 3080–3089 (2013).
29. M. Vallone, M. Goano, F. Bertazzi, G. Ghione, W. Schirmacher, S. Hanna, and H. Figgemeier, "Simulation of small-pitch HgCdTe photodetectors," J. Electron. Mater. **46**, 5458–5470 (2017).
30. M. Vallone, M. Goano, F. Bertazzi, G. Ghione, S. Hanna, D. Eich, and H. Figgemeier, "Diffusive-probabilistic model for inter-pixel crosstalk in HgCdTe focal plane arrays," IEEE J. Electron Devices Soc. **6**, 664–673 (2018).
31. Synopsys, Inc., Mountain View, CA, *Sentaurus Device User Guide. Version N-2017.09* (2017).
32. D. Vasileska, S. M. Goodnick, and G. Klimeck, *Computational Electronics. Semiclassical and Quantum Device Modeling and Simulation* (CRC Press, Boca Raton, FL, 2010).
33. K. Yee, "Numerical solution of initial boundary value problems involving Maxwell's equations in isotropic media," IEEE Trans. Antennas Propag. **14**, 302–307 (1966).
34. M. Born and E. Wolf, *Principles of Optics. Electromagnetic Theory of Propagation, Interference and Diffraction of Light* (Cambridge University Press, Cambridge, U.K., 1999), 7th ed.
35. C. Keasler and E. Bellotti, "Three-dimensional electromagnetic and electrical simulation of HgCdTe pixel arrays," J. Electron. Mater. **40**, 1795–1801 (2011).

36. J. Liang, W. Hu, Z. Ye, L. Liao, Z. Li, X. Chen, and W. Lu, "Improved performance of HgCdTe infrared detector focal plane arrays by modulating light field based on photonic crystal structure," J. Appl. Phys. **115**, 184504 (2014).
37. O. Akın and H.-V. Demir, "High-efficiency low-crosstalk dielectric metasurfaces of mid-wave infrared focal plane arrays," Appl. Phys. Lett. **110**, 143106 (2017).
38. M. Vallone, M. Goano, F. Bertazzi, G. Ghione, W. Schirmacher, S. Hanna, and H. Figgemeier, "Comparing FDTD and ray tracing models in the numerical simulation of HgCdTe LWIR photodetectors," J. Electron. Mater. **45**, 4524–4531 (2016).
39. V. Nathan, "Optical absorption in $Hg_{1-x}Cd_xTe$," J. Appl. Phys. **83**, 2812–2814 (1998).
40. J. Chu and A. Sher, *Physics and Properties of Narrow Gap Semiconductors* (Springer-Verlag, New York, 2008).
41. M. Vallone, M. Mandurrino, M. Goano, F. Bertazzi, G. Ghione, W. Schirmacher, S. Hanna, and H. Figgemeier, "Numerical modeling of SRH and tunneling mechanisms in high-operating-temperature MWIR HgCdTe photodetectors," J. Electron. Mater. **44**, 3056–3063 (2015).
42. M. Mandurrino, G. Verzellesi, M. Goano, M. Vallone, F. Bertazzi, G. Ghione, M. Meneghini, G. Meneghesso, and E. Zanoni, "Trap-assisted tunneling in InGaN/GaN LEDs: experiments and physics-based simulation," in *14th International Conference on Numerical Simulation of Optoelectronic Devices (NUSOD 2014),* (Palma de Mallorca, Spain, 2014), pp. 13–14.
43. M. Mandurrino, M. Goano, M. Vallone, F. Bertazzi, G. Ghione, G. Verzellesi, M. Meneghini, G. Meneghesso, and E. Zanoni, "Semiclassical simulation of trap-assisted tunneling in GaN-based light-emitting diodes," J. Comp. Electron. **14**, 444–455 (2015).
44. M. Mandurrino, G. Verzellesi, M. Goano, M. Vallone, F. Bertazzi, G. Ghione, M. Meneghini, G. Meneghesso, and E. Zanoni, "Physics-based modeling and experimental implications of trap-assisted tunneling in InGaN/GaN light-emitting diodes," Phys. Status Solidi A **212**, 947–953 (2015).
45. E. O. Kane, "Theory of tunneling," J. Appl. Phys. **32**, 83–89 (1961).
46. R. Adar, "Spatial integration of direct band-to-band tunneling currents in general device structures," IEEE Trans. Electron Devices **39**, 976–981 (1992).
47. K. Jóźwikowski, M. Kopytko, A. Rogalski, and A. Jóźwikowska, "Enhanced numerical analysis of current-voltage characteristics of long wavelength infrared n-on-p HgCdTe photodiodes," J. Appl. Phys. **108**, 074519 (2010).
48. G. A. M. Hurkx, D. B. M. Klaassen, and M. P. G. Knuvers, "A new recombination model for device simulation including tunneling," IEEE Trans. Electron Devices **39**, 331–338 (1992).
49. A. Rogalski, *Infrared Detectors* (CRC Press, Boca Raton, FL, 2011), 2nd ed.
50. P. Capper and J. Garland, eds., *Mercury Cadmium Telluride. Growth, Properties and Applications* (John Wiley & Sons, Chichester, U.K., 2011).
51. J.-P. Berenger, "A perfectly matched layer for the absorption of electromagnetic waves," J. Comp. Phys. **114**, 185–200 (1994).
52. Synopsys, Inc., Inc., Optical Solutions Group, Ossining, NY, *RSoft FullWAVE User Guide, v2017.03* (2017).
53. J. Schuster, R. E. DeWames, and P. S. Wijewarnasurya, "Dark currents in a fully-depleted LWIR HgCdTe P-on-n heterojunction: analytical and numerical simulations," J. Electron. Mater. **46**, 6295–6305 (2017).
54. J. Schuster, W. E. Tennant, E. Bellotti, and P. S. Wijewarnasuriya, "Analysis of the Auger recombination rate in $P^+N^-n^-N^-N$ HgCdTe detectors for HOT applications," in *Infrared Technology and Applications XLII,* vol. 9819, Proceedings of the SPIE (2016), p. 98191F.
55. W. Lei, J. Antoszewski, and L. Faraone, "Progress, challenges, and opportunities for HgCdTe infrared materials and detectors," Appl. Phys. Rev. **2**, 041303 (2015).
56. P. Martyniuk, W. Gawron, J. Pawluczyk, A. Keblowski, P. Madejezyk, and A. Rogalski, "Dark current suppression in HOT LWIR HgCdTe heterostructures operating in non-equilibrium mode," J. Infrared Millim. Waves **34**, 385–390 (2015).
57. O. Svelto, *Principles of lasers* (Springer-Verlag, Berlin, 2010), 5th ed.
58. F. Li, J. Deng, J. Zhou, Z. Chu, Y. Yu, X. Dai, H. Guo, L. Chen, S. Guo, M. Lan, and X. Chen, "HgCdTe mid-Infrared photo response enhanced by monolithically integrated meta-lenses," Sci. Rep. **10**, 6372 (2020).